Science Advances
AAAS

Supplementary Materials for

CLIP-Seq analysis enables the design of protective ribosomal RNA bait oligonucleotides against *C9ORF72* ALS/FTD poly-GR pathophysiology

Juan A. Ortega *et al.*

Corresponding author: Evangelos Kiskinis, evangelos.kiskinis@northwestern.edu

Sci. Adv. **9**, eadf7997 (2023)
DOI: 10.1126/sciadv.adf7997

The PDF file includes:

Figs. S1 to S10
Legends for tables S1 to S6

Other Supplementary Material for this manuscript includes the following:

Tables S1 to S6

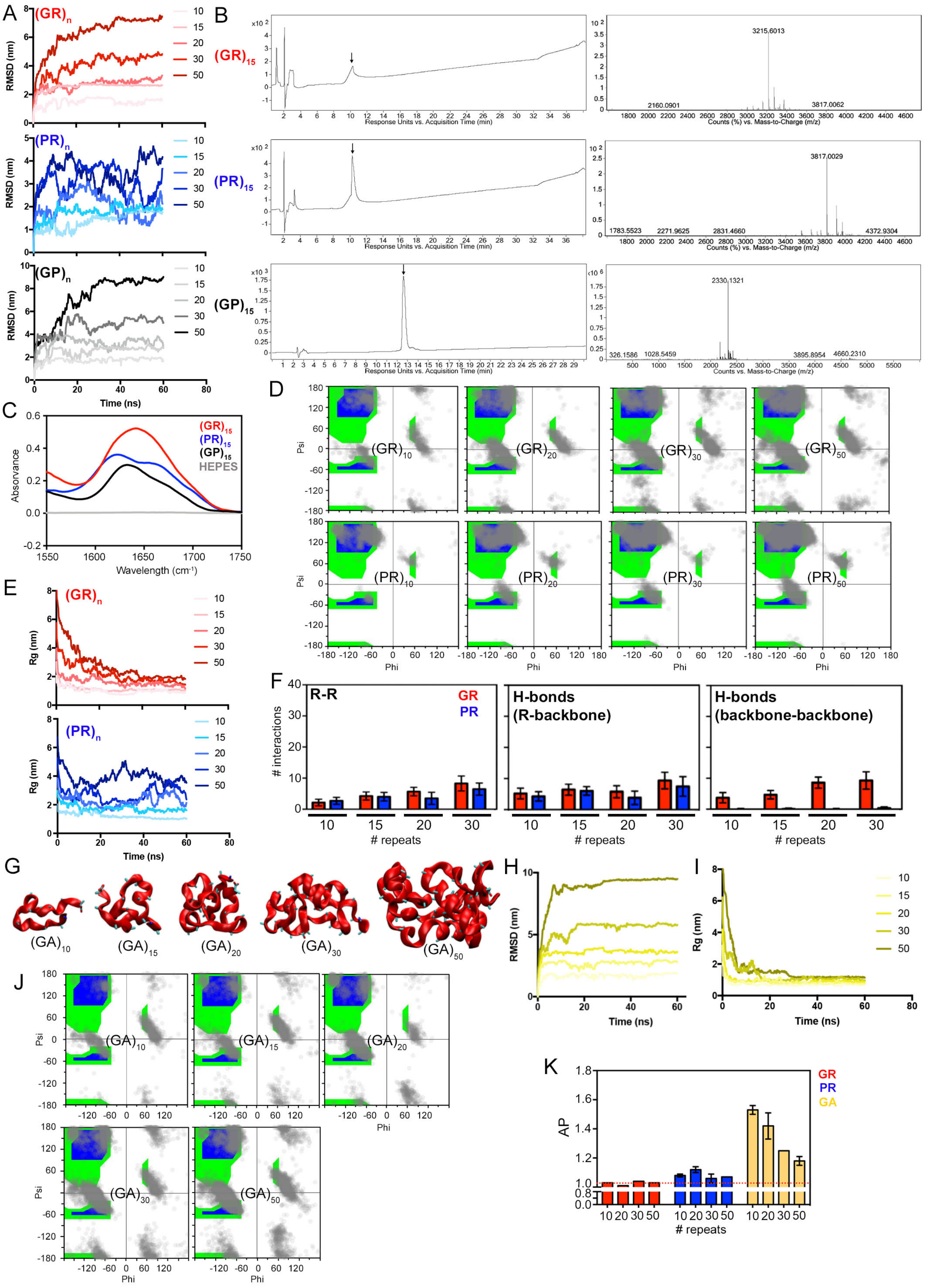
A
(GR)n
RMSD (nm)
10
15
20
30
50
(PR)n
RMSD (nm)
(GP)n
RMSD (nm)
Time (ns)
B
(GR)15
(PR)15
(GP)15
Response Units vs. Acquisition Time (min)
Counts (%) vs. Mass-to-Charge (m/z)
Counts vs. Mass-to-Charge (m/z)
3215.6013
2160.0901
3817.0062
3817.0029
1783.5523
2271.9625
2831.4660
4372.9304
2330.1321
326.1586
1028.5459
3895.8954
4660.2310
C
(GR)15
(PR)15
(GP)15
HEPES
Absorbance
Wavelength (cm-1)
D
(GR)10
(GR)20
(GR)30
(GR)50
(PR)10
(PR)20
(PR)30
(PR)50
Psi
Phi
E
(GR)n
(PR)n
Rg (nm)
Time (ns)
F
R-R
GR
PR
H-bonds (R-backbone)
H-bonds (backbone-backbone)
interactions
repeats
G
(GA)10
(GA)15
(GA)20
(GA)30
(GA)50
H
RMSD (nm)
Time (ns)
I
Rg (nm)
Time (ns)
10
15
20
30
50
J
(GA)10
(GA)15
(GA)20
(GA)30
(GA)50
Psi
Phi
K
AP
GR
PR
GA
repeats

Supplementary Figure 1. Computational and empirical characterization of the physicochemical features of C9 R-DPRs.

A. Line graphs showing changes from the initial structure calculated by root-mean-square deviation (RMSD) over time in $(GR)_n$ (top), $(PR)_n$ (middle), and $(GP)_n$ (bottom) with different repeat number (n=10, 15, 20, 30, 50) in MD simulations.

B. LC-MS chromatograms using UV-vis absorbance (left) and electrospray ionization mass spectrometry (ESI-MS) spectra (right) obtained from pure fractions of synthesized $(GR)_{15}$, $(PR)_{15}$, and $(GP)_{15}$.

C. Line graph showing the secondary structure traces of $(GP)_{15}$, $(GR)_{15}$, and $(PR)_{15}$ analyzed by solid FTIR. Gray line indicates HEPES baseline.

D. Ramachandran plots mapping the secondary structures population present in $(GR)_n$ (top) and $(PR)_n$ (bottom) with different repeat number (n=10, 20, 30, 50).

E. Line graphs representing the radius of gyration (Rg) changes over time in the MD simulations of $(GR)_n$ and $(PR)_n$ with different repeat number (n=10, 15, 20, 30, 50).

F. Bar graphs showing the number of R-R and H-bond (within the backbone or between backbone and R residues) interactions in $(GR)_n$ and $(PR)_n$ with different number of repeats (10, 15, 20, and 30). Values represent mean ± SD.

G. All-atoms MD simulation of the secondary structure of $(GA)_n$ with different repeat number (n=10, 15, 20, 30, 50).

H. Line graph showing the changes from the initial structure calculated by RMSD over time in $(GA)_n$ with different repeat number (n=10, 15, 20, 30, 50).

I. Line graph representing the Rg changes over time in the MD simulations of $(GA)_n$ with different repeat number (n=10, 15, 20, 30, 50).

J. Ramachandran plots mapping the secondary structures population present in $(GA)_n$ with different repeat number (n=10, 15, 20, 30, 50).

K. Bar graph showing coarse-grained MD simulation-based aggregation propensity (AP) calculated for $(GR)_n$, $(PR)_n$, and $(GA)_n$ (n=10, 20, 30, 50). Red dashed line indicates the average AP values calculated in poly-GR. Values represent mean ± SD.

Raw data of all the simulations presented in this figure can be found in Table S1.

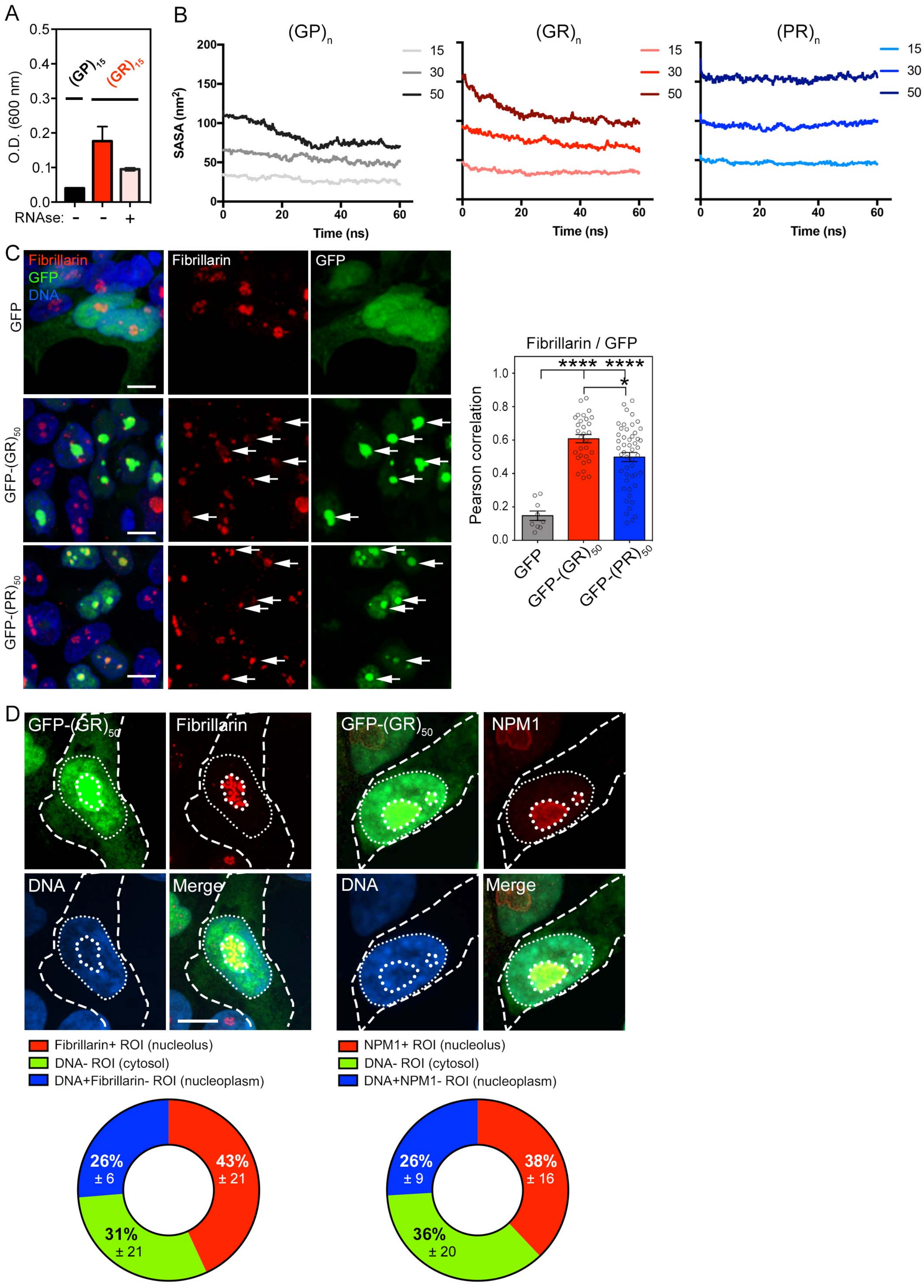
A
O.D. (600 nm)
0.0
0.1
0.2
0.3
0.4
0.5
(GP)15
(GR)15
RNAse: - - +
B
(GP)n
(GR)n
(PR)n
SASA (nm2)
0
50
100
150
200
Time (ns)
0
20
40
60
15
30
50
C
Fibrillarin
GFP
DNA
GFP
GFP-(GR)50
GFP-(PR)50
Fibrillarin / GFP
Pearson correlation
0.0
0.2
0.4
0.6
0.8
1.0
****
****
*
GFP
GFP-(GR)50
GFP-(PR)50
D
GFP-(GR)50
Fibrillarin
DNA
Merge
NPM1
Fibrillarin+ ROI (nucleolus)
DNA- ROI (cytosol)
DNA+Fibrillarin- ROI (nucleoplasm)
NPM1+ ROI (nucleolus)
DNA+NPM1- ROI (nucleoplasm)
26%
± 6
43%
± 21
31%
± 21
26%
± 9
38%
± 16
36%
± 20

Supplementary Figure 2. Characterization of the interaction between R-DPRs and RNA *in vitro,* and localization of R-DPRs in cells.

A. Bar plot showing turbidity assay measurements utilized to assess the level of interaction of $(GR)_{15}$ with total human RNA in the absence/presence of RNase. $(GP)_{15}$ was used as a reference as it does not bind to RNA.

B. Line graphs representing the SASA changes over time in MD simulations of $(GP)_n$, $(GR)_n$, and $(PR)_n$ with different number of repeats (n=15, 30, 50).

C. Left: Confocal images of HEK-293 cells transfected with GFP, GFP-$(GR)_{50}$, or GFP-$(PR)_{50}$ and labeled for the nucleolar marker fibrillarin using immunocytochemistry. Scale bar = 15 μm. Right: Dot plot showing the level of colocalization of fibrillarin with GFP and GFP-fused R-DPRs. Each dot in graph represents a single cell. Bars represented the mean ± standard error mean (SEM); ANOVA p*<0.05; ****<0.0001.

D. Top: Confocal images of HEK-293 cells transfected with GFP-$(GR)_{50}$ and immunostained for Fibrillarin or Nucleophosmin (NPM1), which label the fibrillar and granular components of the nucleolus, respectively. DNA was visualized by staining with Hoechst 33342. Scale bar = 10 μm Dashed lines indicate cytosolic borders, while thin and thick pointed lines depict nuclear and nucleolar borders, respectively. Bottom: Pie charts displaying the distribution of the GFP-$(GR)_{50}$ signal within the different subcellular compartments (cytosol, nucleoplasm, and nucleolus) defined by the selected markers. ROI: region of interest. Values are presented as the mean ± standard error mean (SEM).

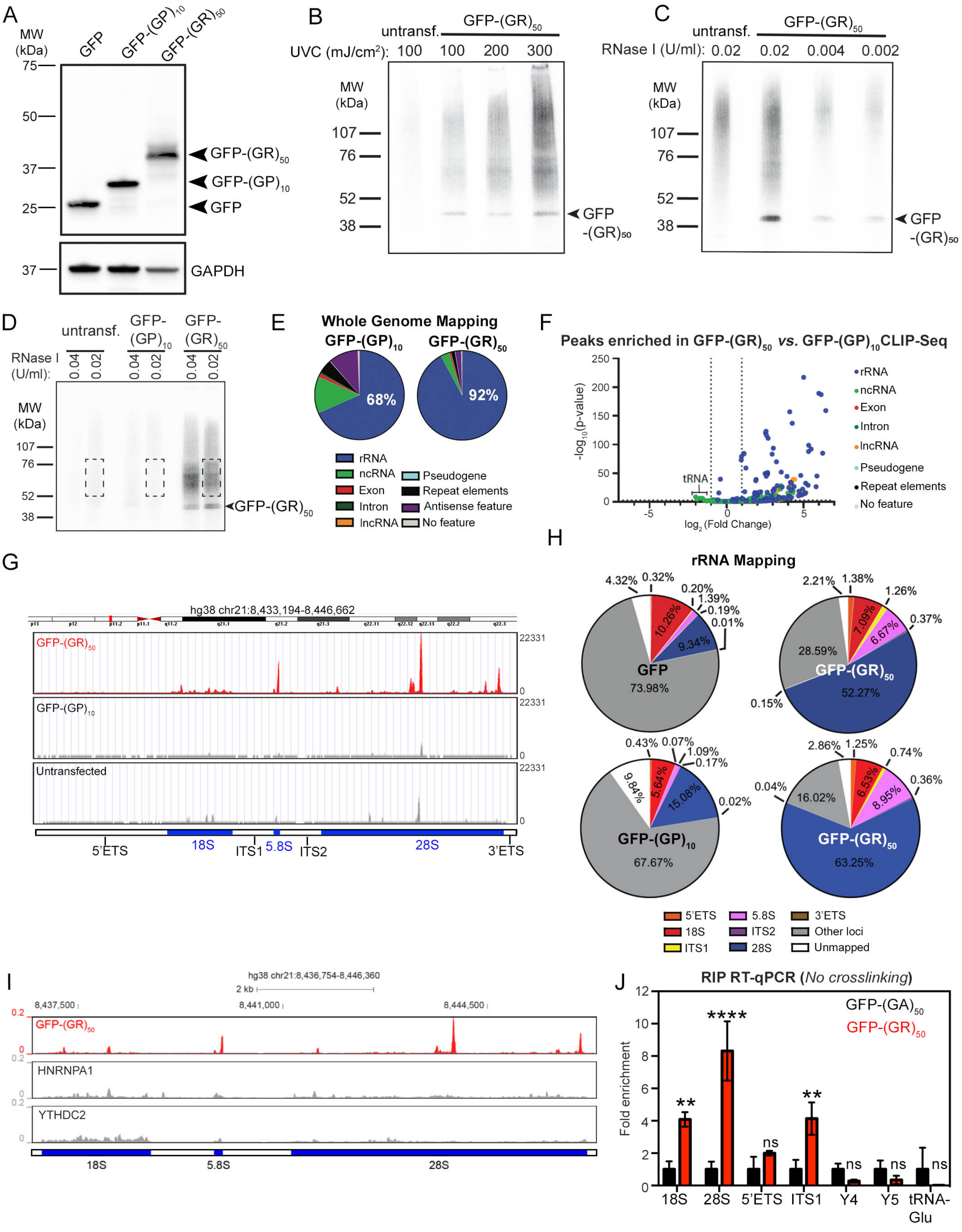
A
MW (kDa)
GFP
GFP-(GP)$_{10}$
GFP-(GR)$_{50}$
75
50
37
25
GFP-(GR)$_{50}$
GFP-(GP)$_{10}$
GFP
37
GAPDH
B
untransf.
GFP-(GR)$_{50}$
UVC (mJ/cm^2): 100 100 200 300
MW (kDa)
107
76
52
38
GFP -(GR)$_{50}$
C
untransf.
GFP-(GR)$_{50}$
RNase I (U/ml): 0.02 0.02 0.004 0.002
MW (kDa)
107
76
52
38
GFP -(GR)$_{50}$
D
untransf.
GFP-(GP)$_{10}$
GFP-(GR)$_{50}$
RNase I (U/ml):
0.04 0.02 0.04 0.02 0.04 0.02
MW (kDa)
107
76
52
38
GFP-(GR)$_{50}$
E
Whole Genome Mapping
GFP-(GP)$_{10}$
GFP-(GR)$_{50}$
68%
92%
rRNA
ncRNA
Exon
Intron
lncRNA
Pseudogene
Repeat elements
Antisense feature
No feature
F
Peaks enriched in GFP-(GR)$_{50}$ vs. GFP-(GP)$_{10}$CLIP-Seq
-log$_{10}$(p-value)
250
200
150
100
50
0
tRNA
-5
0
5
log$_2$ (Fold Change)
rRNA
ncRNA
Exon
Intron
lncRNA
Pseudogene
Repeat elements
No feature
G
hg38 chr21:8,433,194-8,446,662
GFP-(GR)$_{50}$
GFP-(GP)$_{10}$
Untransfected
22331
0
5'ETS
18S
ITS1
5.8S
ITS2
28S
3'ETS
H
rRNA Mapping
GFP
4.32% 0.32% 0.20% 1.39% 0.19% 0.01%
10.26%
9.34%
73.98%
GFP-(GR)$_{50}$
2.21% 1.38% 1.26% 0.37%
7.09%
6.67%
28.59%
0.15%
52.27%
GFP-(GP)$_{10}$
0.43% 0.07% 1.09% 0.17%
9.84%
5.64%
15.08%
0.02%
67.67%
GFP-(GR)$_{50}$
2.86% 1.25% 0.74% 0.36%
0.04%
16.02%
6.53%
8.95%
63.25%
5'ETS
18S
ITS1
5.8S
ITS2
28S
3'ETS
Other loci
Unmapped
I
hg38 chr21:8,436,754-8,446,360
2 kb
8,437,500
8,441,000
8,444,500
0.2
0
GFP-(GR)$_{50}$
HNRNPA1
YTHDC2
18S
5.8S
28S
J
RIP RT-qPCR (No crosslinking)
GFP-(GA)$_{50}$
GFP-(GR)$_{50}$
Fold enrichment
12
10
8
6
4
2
0
**
****
ns
**
ns
ns
ns
18S
28S
5'ETS
ITS1
Y4
Y5
tRNA-Glu

Supplementary Figure 3. Characterization of the interactions between poly-GR and RNA in live cells.

A. Lysates of HEK-293 cells transfected with GFP, GFP-$(GP)_{10}$ or GFP-$(GR)_{50}$ were subjected to western blot (WB) to detect GFP. GAPDH is a loading control.

B. After crosslinking HEK-293 cells expressing GFP-$(GR)_{50}$ with increasing doses of UV (254 nm) and IP with anti-GFP antibodies, RNPs were labeled with [γ-^{32}P]-ATP, fractionated by SDS-PAGE, transferred to a membrane, and detected by autoradiography. Untransfected cells were controls. Arrow indicates the GFP-$(GR)_{50}$ band.

C. Lysates of UV-crosslinked untransfected HEK-293 cells and cells expressing GFP-$(GR)_{50}$ were incubated with the indicated amounts of RNase I prior to IP and analysis as in (**B**). Arrow indicates the GFP-$(GR)_{50}$ band.

D. After UV crosslinking, HEK-293 cells expressing GFP, GFP-$(GP)_{10}$ or GFP-$(GR)_{50}$ were lysed, treated with the indicated amounts of RNase I and immunoprecipitated with anti-GFP antibodies. RNPs in immunoprecipitates were labeled with [γ-^{32}P]-ATP and detected as in (**B)**. Dashed lines indicate RNPs excised for library preparation. Arrow indicates the GFP-$(GR)_{50}$ band.

E. Pie charts indicating the percentage of CLIP-Seq (replicate #2) peaks in the indicated classes of RNAs in GFP-$(GP)_{10}$ and GFP-$(GR)_{50}$ samples. Peaks were defined as having at least 5 overlapping reads.

F. Volcano plot showing CLIP-Seq peaks enriched in GFP-$(GR)_{50}$ compared to GFP-$(GP)_{10}$ in CLIP-Seq (replicate #2). Negative $\log_2$ (fold change) indicates peaks that were more abundant in the GFP-$(GP)_{10}$ control. As in replicate #1, GFP-$(GR)_{50}$-CLIP-Seq peaks are enriched for rRNA, while tRNA peaks are more abundant in the control.

G. Distribution of reads mapping to the RNA45SN1 locus from the GFP-$(GR)_{50}$ (top), GFP-$(GP)_{10}$ (middle), and untransfected (bottom) CLIP-Seq (replicate #2) analyses.

H. Reads from the GFP, GFP-$(GP)_{10}$, and GFP-$(GR)_{50}$ CLIP-Seq (replicates #1 and #2) analyses were mapped to the RNA45SN1 locus. Reads that did not map to this locus were re-mapped to the hg38 human genome to determine the fraction that mapped to other genomic loci. Reads that did not map to hg38 are designated as “unmapped”. The percentage of reads in each category was quantified as a percentage of the total reads.

I. Distribution of reads mapping to the RNA45SN1 locus from CLIP-Seq analyses after IP for GFP-$(GR)_{50}$ (top), HNRNPA1 (middle), and YTHDC2 (bottom).

J. After IP, the levels of the indicated RNAs in anti-GFP-$(GA)_{50}$ and anti-GFP-$(GR)_{50}$ immunoprecipitates were measured by RT-qPCR. The fold-enrichment of each RNA relative to the anti-GFP control is shown. n=2 independent biological replicates; Values are presented as the mean ± SEM; Two-Way ANOVA, $p^{**} < 0.01$; $^{****} < 0.0001$; ns, not significant.

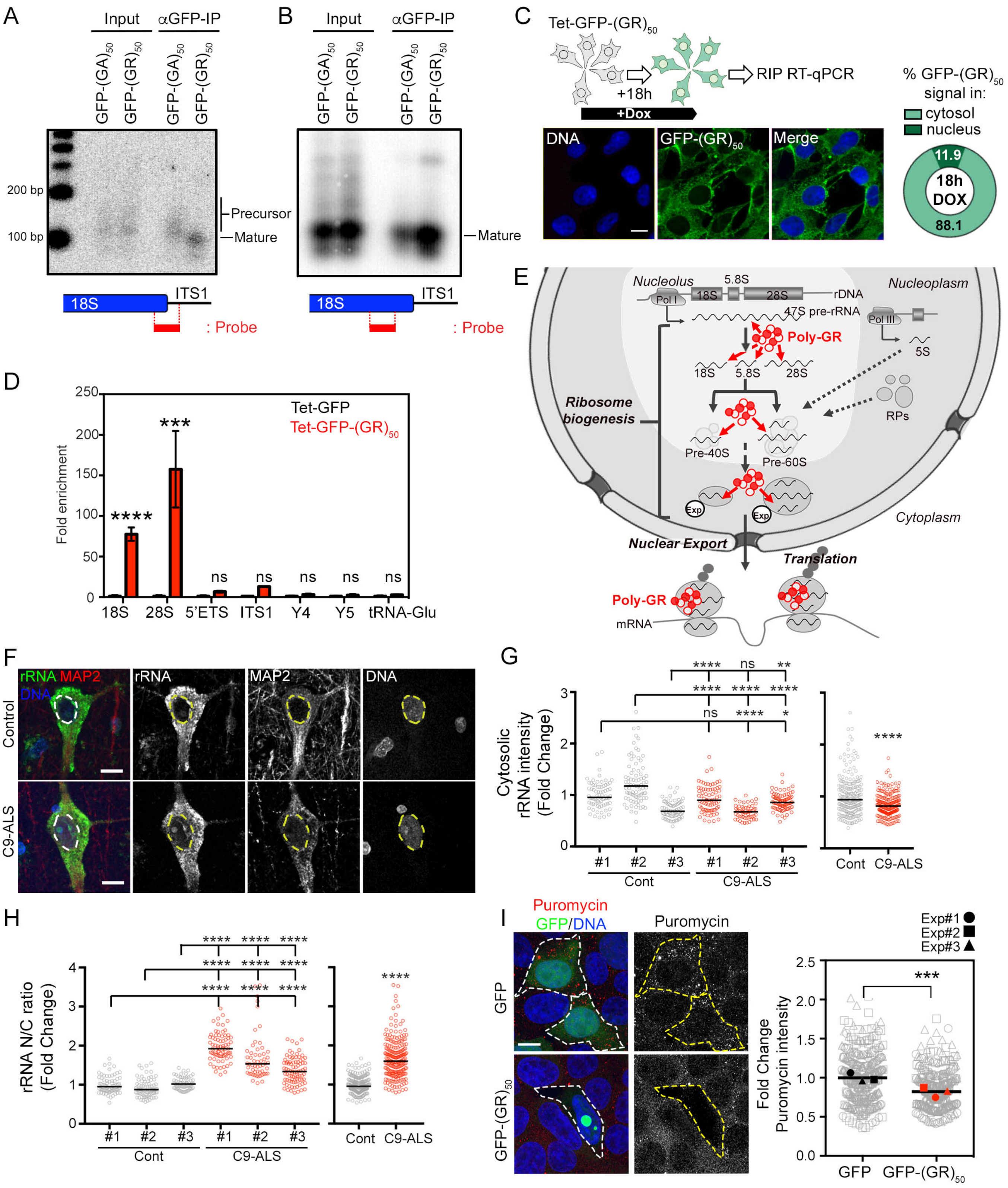
A
Input
αGFP-IP
GFP-(GA)$_{50}$
GFP-(GR)$_{50}$
GFP-(GA)$_{50}$
GFP-(GR)$_{50}$
200 bp
100 bp
Precursor
Mature
18S
ITS1
: Probe
B
Input
αGFP-IP
GFP-(GA)$_{50}$
GFP-(GR)$_{50}$
GFP-(GA)$_{50}$
GFP-(GR)$_{50}$
Mature
18S
ITS1
: Probe
C
Tet-GFP-(GR)$_{50}$
+18h
+Dox
RIP RT-qPCR
DNA
GFP-(GR)$_{50}$
Merge
% GFP-(GR)$_{50}$ signal in:
cytosol
nucleus
11.9
18h DOX
88.1
D
Fold enrichment
250
200
150
100
50
0
Tet-GFP
Tet-GFP-(GR)$_{50}$
****
***
ns
ns
ns
ns
ns
18S
28S
5'ETS
ITS1
Y4
Y5
tRNA-Glu
E
Nucleolus
5.8S
18S
28S
rDNA
Pol I
47S pre-rRNA
Nucleoplasm
Pol III
5S
Poly-GR
18S
5.8S
28S
Ribosome biogenesis
RPs
Pre-40S
Pre-60S
Exp
Exp
Cytoplasm
Nuclear Export
Translation
Poly-GR
mRNA
F
rRNA MAP2 DNA
rRNA
MAP2
DNA
Control
C9-ALS
G
Cytosolic rRNA intensity (Fold Change)
3
2
1
0
****
ns
**
****
****
****
ns
****
*
#1
#2
#3
#1
#2
#3
Cont
C9-ALS
****
Cont
C9-ALS
H
rRNA N/C ratio (Fold Change)
4
3
2
1
0
****
****
****
****
****
****
****
****
****
#1
#2
#3
#1
#2
#3
Cont
C9-ALS
****
Cont
C9-ALS
I
Puromycin
GFP/DNA
Puromycin
GFP
GFP-(GR)$_{50}$
Exp#1 ●
Exp#2 ■
Exp#3 ▲
Fold Change Puromycin intensity
2.5
2.0
1.5
1.0
0.5
0.0
***
GFP
GFP-(GR)$_{50}$

Supplementary Figure 4. Poly-GR binds to multiple ribosomal RNA species in live cells.

A. and **B**. Lysates of HEK-293 cells expressing GFP-$(GA)_{50}$ or GFP-$(GR)_{50}$ were subjected to IP with anti-GFP antibodies. The isolated RNA was used in 3' RACE and the resulting cDNAs subjected to Southern blotting and probed with the indicated oligonucleotides to preferentially detect 3'-extended (A) and mature (B)18S rRNAs.

C. Top: Schematic of the doxycycline-inducible GFP-$(GR)_{50}$ expression system utilized to determine the level of interaction of poly-GR with cytosolic rRNA/ribosomes. Bottom: Confocal images of Doxycycline-induced expression of GFP-$(GR)_{50}$ in HEK-293 cells, after 18h of induction. Hoechst 33342 was used to counterstain nuclei. Scale bar= 10μm. Right: Pie chart showing the distribution of the GFP-$(GR)_{50}$ signal within the nucleus or cytosol after 18h of doxycycline induction.

D. After IP, the levels of the indicated RNAs in anti-GFP and anti-GFP-$(GR)_{50}$ immunoprecipitates were measured by RT-qPCR. The fold-enrichment of each RNA relative to the anti-GFP control is shown. n=2 independent biological replicates; Values are presented as the mean ± SEM; Two-Way ANOVA, ***<0.001; ****<0.0001; ns, not significant.

E. Schematic model summarizing poly-GR interactions with rRNA and the potential consequences, including defects in ribosome biogenesis and protein translation.

F. Representative immunohistochemistry confocal images of layer V neurons immunolabeled for rRNA (green), MAP2 (red), and DNA (blue) in motor cortex tissue from a non-neurological control and a C9-ALS patient. Scale bars= 10μm.

G. Left: Dot plot displaying cytosolic rRNA intensity of rRNA signal observed in cortical neurons of three non-neurological age-matched controls and three C9-ALS patients. Compiled control (n=225 cells) vs. C9-ALS (n=218 cells) data is shown on the right dot plot. Bars represent median; ANOVA followed by Kruskal-Wallis rank test (left) and Mann-Whitney U test (right), p *<0.05, **<0.01, ****<0.0001. ns, not significant.

H. Left: Dot plot displaying the fold change in the N/C ratio of rRNA signal observed in cortical neurons of three non-neurological age-matched controls and three C9-ALS patients. Compiled control (n=225 cells) vs. C9-ALS (n=218 cells) data is shown on the right dot plot. Bars represent median; ANOVA followed by Kruskal-Wallis rank test (left) and Mann-Whitney U test (right), p****<0.0001.

I. Left: Confocal images of GFP- and GFP-$(GR)_{50}$-transfected HEK-293 cells immunolabeled for puromycin. Hoechst 33342 was used to counterstain nuclei. Scale bar= 20μm. Right: Dot plot showing the fluorescence intensity of puromycin staining in GFP- and GFP-$(GR)_{50}$-transfected HEK-293 cells (n=324 cells/condition). Individual cells from 3 experiments are represented by distinct shaped symbols in grey, median values of each experiment are represented by distinct shaped symbols in color, and bars represent the global median per condition. Multiple Comparisons of Means: Tukey contrasts test, p***<0.001.

A

Radwan et al., 2020	Hatmann et al.,2018 HEK-293	Hatmann et al.,2018 rodent cortical neurons	Lopez-Gonzalez et al.,2016	Lee et al., 2016	Yin et al., 2017	Tao et al., 2015	**Ribosomal proteins**
●	●	●	●	●	●	●	**RPL7A**
●	●	●	●	●	●		RPS2; RPL6; RPL5; RPL3
●	●	●		●	●	●	RPL4
●	●	●	●		●		RPS15
●	●		●		●		RPL18; RPS9; RPS18; RPS8; RPS24
●			●	●	●	●	RPS6
●	●	●		●	●		RPS25; RPL12; RPS19; RPL7; RPS7
●	●	●	●	●			RPL15
	●		●	●	●		RPL19
●	●		●		●		RPL32; RPL34; RPL35A; RPL18A; RPL31
●			●	●	●		RPL10; RPL24; RPL17; RPL13
	●	●		●	●		RPSA; RPL23A
●	●	●			●		P2; RPL10A; P0
●	●				●		RPS11; RPS3A; RPS16; RPL22; RPL14; RPS20; RPL11; RPS12; RPS13; RPS3; RPS15A; RPS5
		●	●		●		RPL28
	●		●		●		RPL8
●			●		●		RPL26; RPS23; RPL13A
	●	●			●		RPS27
●	●				●		RPL27; RPL35; RPL27A; RPL30
●				●	●		RPS14
	●	●	●				RPL36
●	●	●					P1
●	●			●			RPS10
	●			●			RPL38; RPL29
				●	●		RPL23
	●		●				RPS21
●			●				RPL21; RPS27
●	●						RPS17; RPS28; RPS29
					●		RPL9
		●					RPL36A
●							RPS21; RPS4

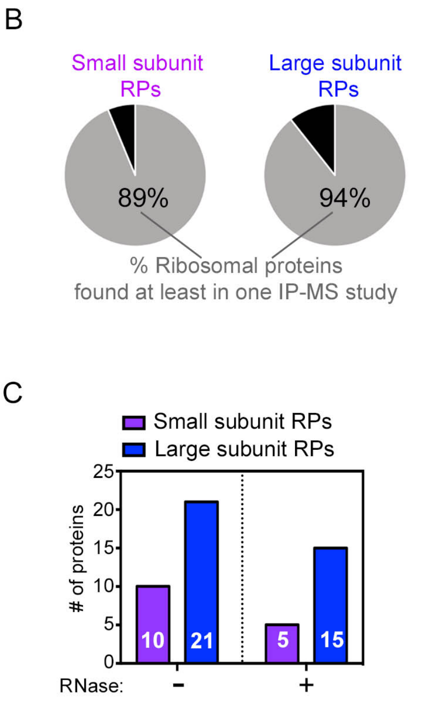

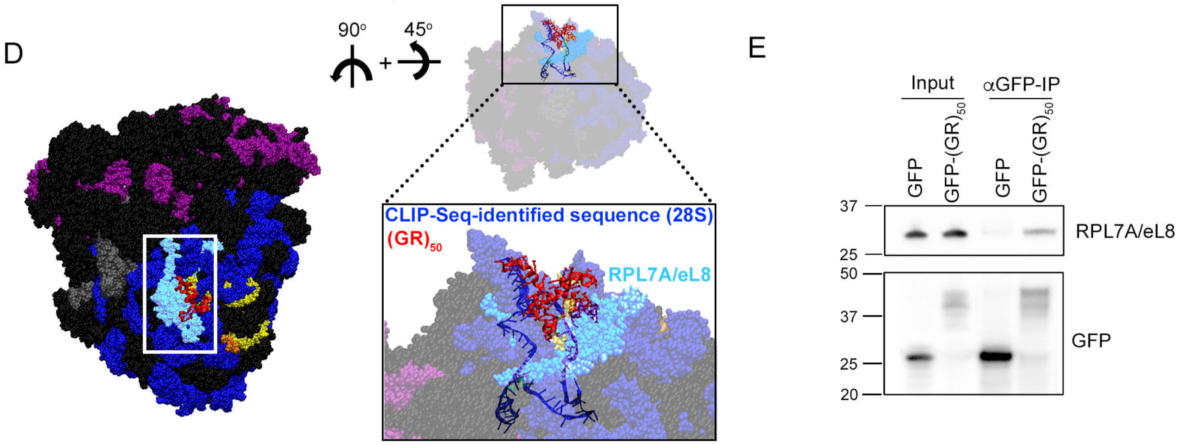

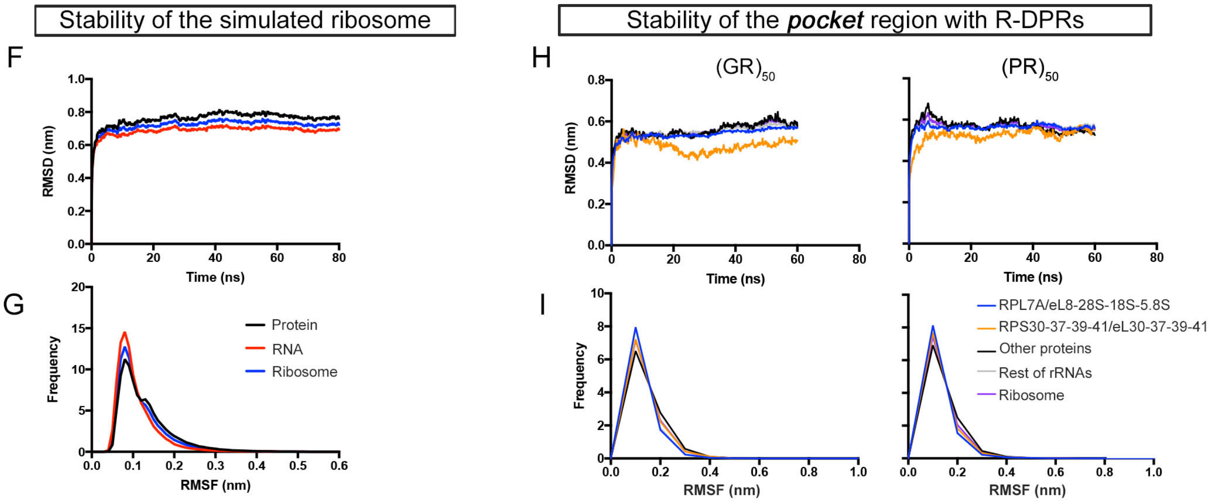

Supplementary Figure 5. Computational modeling of poly-GR binding to ribosomal RNA and protein subunits.

A. Comparative data analysis of the RPs detected in published datasets of IP-MS experiments performed in mammalian *in vitro* cell models. Red dots indicate a positive interaction of poly-GR with the respective RPs.

B. Pie charts showing the percentage of small and large ribosomal subunit proteins immunoprecipitated with poly-GR in at least one previous study.

C. Bar graphs displaying the number of small (purple) and large (blue) ribosomal subunit proteins immunoprecipitated with poly-GR in the presence or absence of RNase as described by (*44*).

D. Left: All-atoms MD simulation of the mammalian 80S ribosome showing a putative region (indicated by a white line box) of interaction with $(GR)_{50}$ (pocket). The RPs and RNAs surrounding this region are labeled as follows: RPL7A: turquoise; RPS30/RPL37/RPL39/RPL41: orange; 28S: blue; 5.8S: yellow; 18S: purple; Other proteins and RNAs are labeled in black and gray respectively. $(GR)_{50}$ is colored in red. Right: A different angle of view of the mammalian ribosome reflects the close proximity between the 28S sequence identified by our CLIP-Seq analysis and RPL7A/eL8, consistently detected as a $(GR)_{50}$-interactor by 7 independent IP-MS studies. Angle of view with respect to the image on the left is represented at the top left part of the panel.

E. IP-WB analysis of GFP-$(GR)_{50}$ or GFP in HEK-293 transfected cells. Cell lysates were subjected to IP with anti-GFP antibodies and WB was performed to detect RPL7A/eL8 (top) and GFP (bottom).

F. Line graph showing changes from the initial structure calculated by RMSD over time in the different components of the mammalian ribosome.

G. Line graph showing the frequency of changes calculated by root-mean-square fluctuation (RMSF) of the last 10 ns in the different components of the mammalian ribosome.

H. Line graphs showing changes from the initial structure calculated by RMSD over time in the RNA and protein components of the "*pocket"* region of the mammalian ribosome in the presence of $(GR)_{50}$ and $(PR)_{50}$.

I. Line graphs showing the frequency of changes calculated by RMSF of the last 10 ns in the different components of the mammalian ribosomal "*pocket"* region in the presence of $(GR)_{50}$ and $(PR)_{50}$.

Raw data of all the simulations presented in this figure can be found in Table S4.

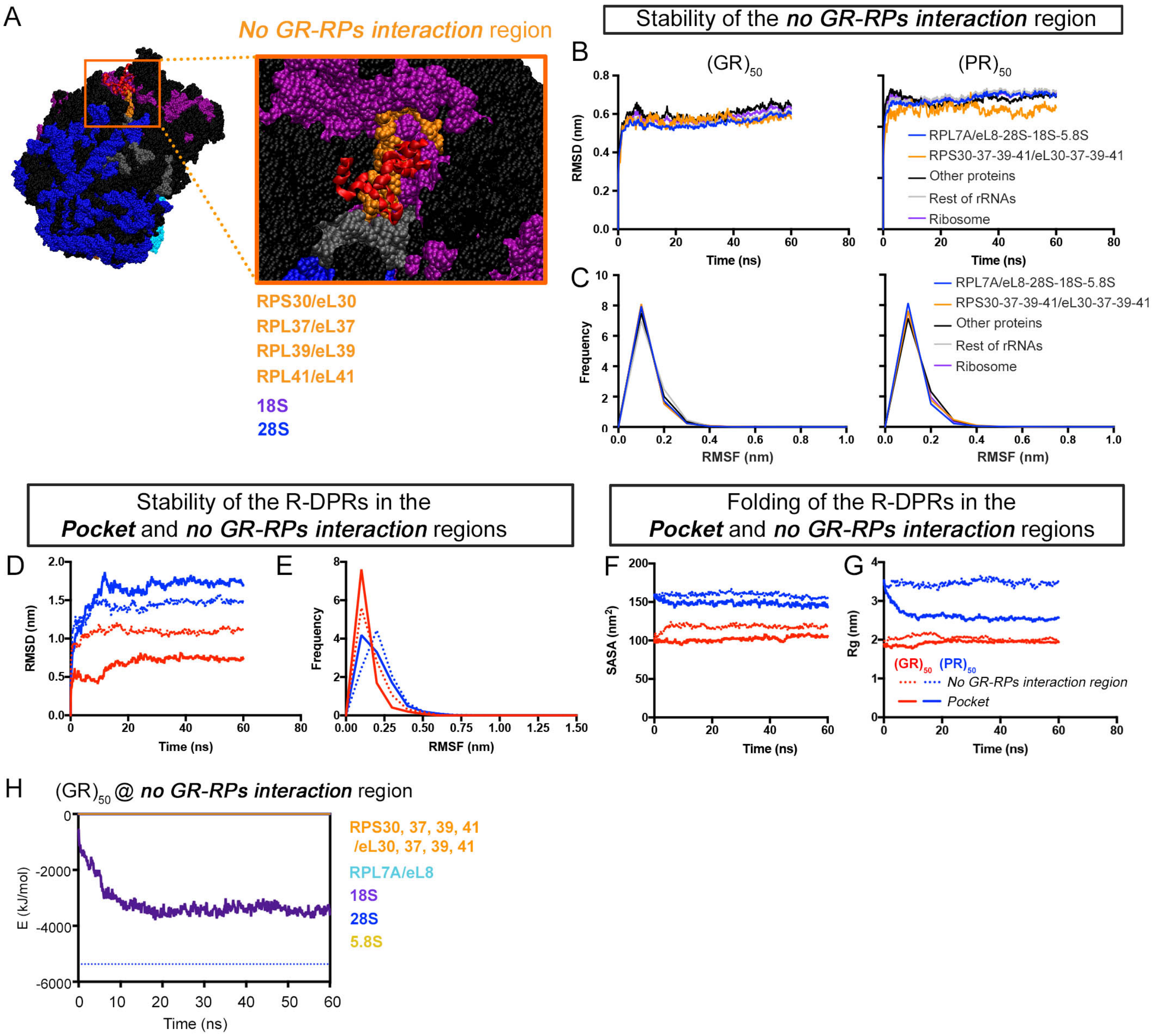
A
No GR-RPs interaction region
RPS30/eL30
RPL37/eL37
RPL39/eL39
RPL41/eL41
18S
28S
Stability of the no GR-RPs interaction region
B
(GR)50
(PR)50
RMSD (nm)
0.0
0.2
0.4
0.6
0.8
Time (ns)
0
20
40
60
80
RPL7A/eL8-28S-18S-5.8S
RPS30-37-39-41/eL30-37-39-41
Other proteins
Rest of rRNAs
Ribosome
C
Frequency
0
2
4
6
8
10
RMSF (nm)
0.0
0.2
0.4
0.6
0.8
1.0
Stability of the R-DPRs in the Pocket and no GR-RPs interaction regions
D
RMSD (nm)
0.0
0.5
1.0
1.5
2.0
Time (ns)
E
Frequency
RMSF (nm)
0.00
0.25
0.50
0.75
1.00
1.25
1.50
Folding of the R-DPRs in the Pocket and no GR-RPs interaction regions
F
SASA (nm²)
0
50
100
150
200
Time (ns)
G
Rg (nm)
0
1
2
3
4
Time (ns)
(GR)50
(PR)50
No GR-RPs interaction region
Pocket
H
(GR)50 @ no GR-RPs interaction region
E (kJ/mol)
0
-2000
-4000
-6000
Time (ns)
0
10
20
30
40
50
60
RPS30, 37, 39, 41 /eL30, 37, 39, 41
RPL7A/eL8
18S
28S
5.8S

Supplementary Figure 6. Computational modeling of poly-GR binding to ribosomal RNA and protein subunits.

A. Representative image recreated by all-atoms MD simulations of $(GR)_{50}$ and $(PR)_{50}$ interacting with distinct rRNAs and RPs present in the "*no GR-RPs interaction"* region magnified in the inset on the right. Based on 7 different IP-MS studies, the proteins in this ribosomal region do not interact with poly-GR.

B. Line graphs showing changes from the initial structure calculated by RMSD over time in the RNA and protein components of the "*no GR-RPs interaction"* region of the mammalian ribosome in the presence of $(GR)_{50}$ (left) and $(PR)_{50}$ (right).

C. Line graphs showing the frequency of changes calculated by RMSF of the last 10 ns in the RNA and protein components of the "*no GR-RPs interaction"* region of the mammalian ribosome in the presence of $(GR)_{50}$ (left) and $(PR)_{50}$ (right).

D. Line graph showing changes from the initial structure calculated by RMSD over time of $(GR)_{50}$ and $(PR)_{50}$ in the "*pocket"* and "*no GR-RPs interaction"* region of the mammalian ribosome.

E. Line graph showing the frequency of changes calculated by RMSF of the last 10 ns for $(GR)_{50}$ and $(PR)_{50}$ in the "*pocket"* and "*no GR-RPs interaction"* region of the mammalian ribosome.

F. Line graph representing the SASA value changes over time of $(GR)_{50}$ and $(PR)_{50}$ in the "*pocket"* and "*no GR-RPs interaction"* region of the mammalian ribosome.

G. Line graph representing the Rg changes over time of $(GR)_{50}$ and $(PR)_{50}$ in the "*pocket"* and "*no GR-RPs interaction"* region of the mammalian ribosome.

H. Line graph indicating the energetic strength of the interactions of $(GR)_{50}$ in the "*no GR-RPs interaction"* region of the ribosome over time. Dashed line indicates the highest interaction energy achieved between $(GR)_{50}$ and 28S rRNA.

Raw data of all the simulations presented in this figure can be found in Table S4.

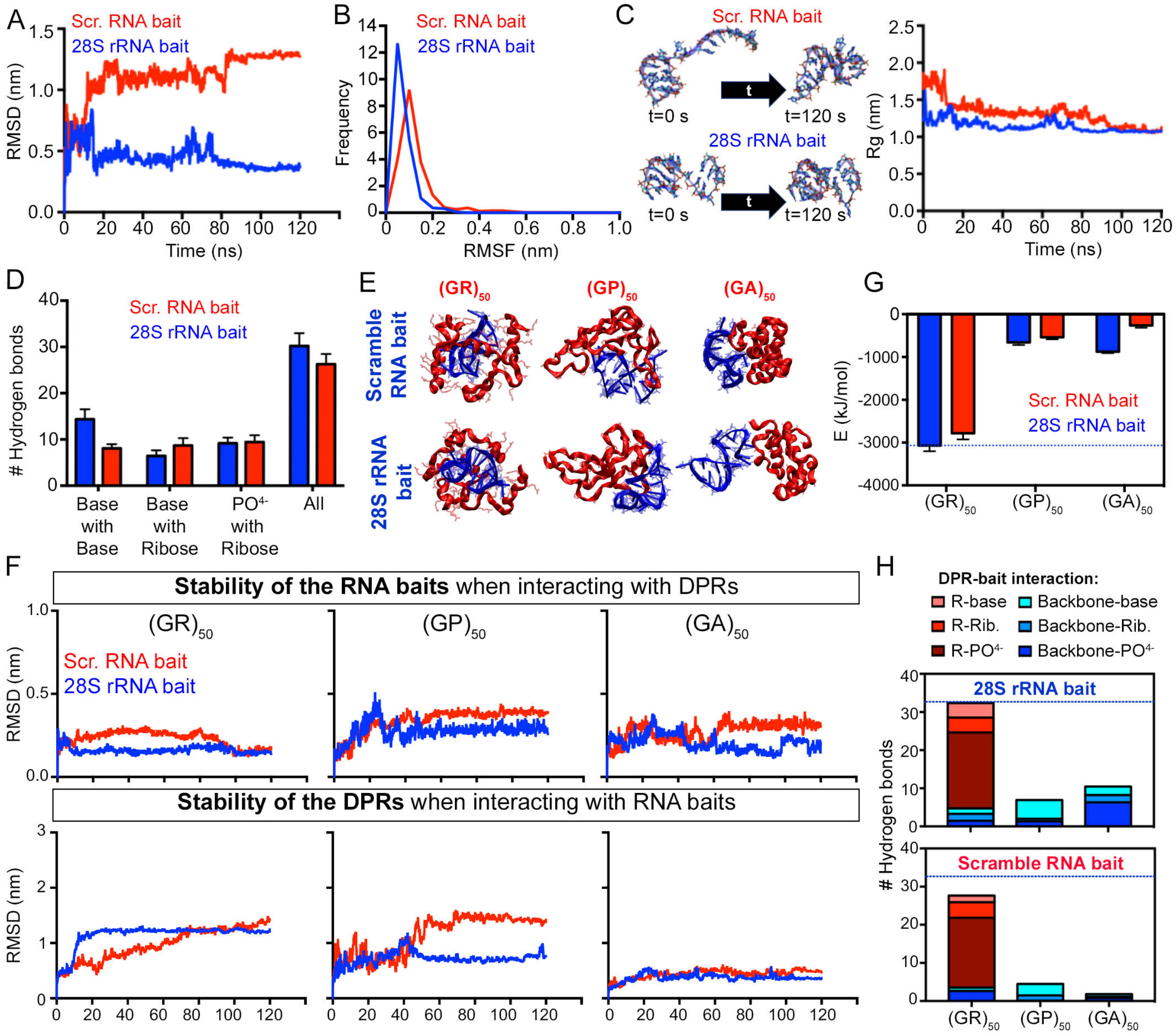
A
Scr. RNA bait
28S rRNA bait
RMSD (nm)
Time (ns)
B
Frequency
RMSF (nm)
Scr. RNA bait
28S rRNA bait
C
Scr. RNA bait
t=0 s
t
t=120 s
28S rRNA bait
t=0 s
t
t=120 s
Rg (nm)
Time (ns)
D
Scr. RNA bait
28S rRNA bait
Hydrogen bonds
Base with Base
Base with Ribose
PO4- with Ribose
All
E
(GR)50
(GP)50
(GA)50
Scramble RNA bait
28S rRNA bait
G
E (kJ/mol)
Scr. RNA bait
28S rRNA bait
(GR)50
(GP)50
(GA)50
F
Stability of the RNA baits when interacting with DPRs
(GR)50
(GP)50
(GA)50
Scr. RNA bait
28S rRNA bait
RMSD (nm)
Stability of the DPRs when interacting with RNA baits
RMSD (nm)
H
DPR-bait interaction:
R-base
R-Rib.
R-PO4-
Backbone-base
Backbone-Rib.
Backbone-PO4-
28S rRNA bait
Scramble RNA bait
Hydrogen bonds
(GR)50
(GP)50
(GA)50

Supplementary Figure 7. Modified RNA-based strategy to inhibit the toxic effects of poly-GR on ribosomal homeostasis.

A. Line graph showing changes from the initial structure calculated by RMSD over time in the scrambled and 28S rRNA baits.

B. Line graph showing the frequency of changes calculated by RMSF of the last 10 ns in the scrambled and 28S rRNA baits.

C. Line graph (right) representing the Rg changes over time in the MD simulations of the scrambled and 28S rRNA baits (left).

D. Bar plot showing the number of hydrogen bonds established in the secondary structure of scrambled and 28S rRNA baits between bases, bases and ribose groups, or PO^{4-} and ribose groups. The values are presented as the mean ± SD.

E. MD simulation snapshots showing how differential secondary structures of scrambled and 28S rRNA baits interact with distinct DPRs.

F. Top: Line graphs showing changes from the initial structure calculated by RMSD over time of scrambled and 28S baits upon interaction with DPRs. Bottom: Line graphs showing changes from the initial structure calculated by RMSD over time of $(GR)_{50}$, $(GP)_{50}$, and $(GA)_{50}$ upon interaction with scrambled and 28S rRNA baits.

G. Bar graph showing average energy of interaction of scrambled and 28S baits with distinct DPRs during the last 10 ns, when structure is considered stable. Values are presented as mean ± SD. Blue dashed line indicates the highest interaction energy achieved between $(GR)_{50}$ and the 28S rRNA bait.

H. Bar plots showing the number of hydrogen bonds established between the bases, ribose, or PO^{4-} groups of scrambled or 28S rRNA baits, and the backbone or R residues of distinct DPRs. The values are presented by mean values. Blue dashed line indicates the highest interaction energy achieved between $(GR)_{50}$ and the 28S rRNA bait.

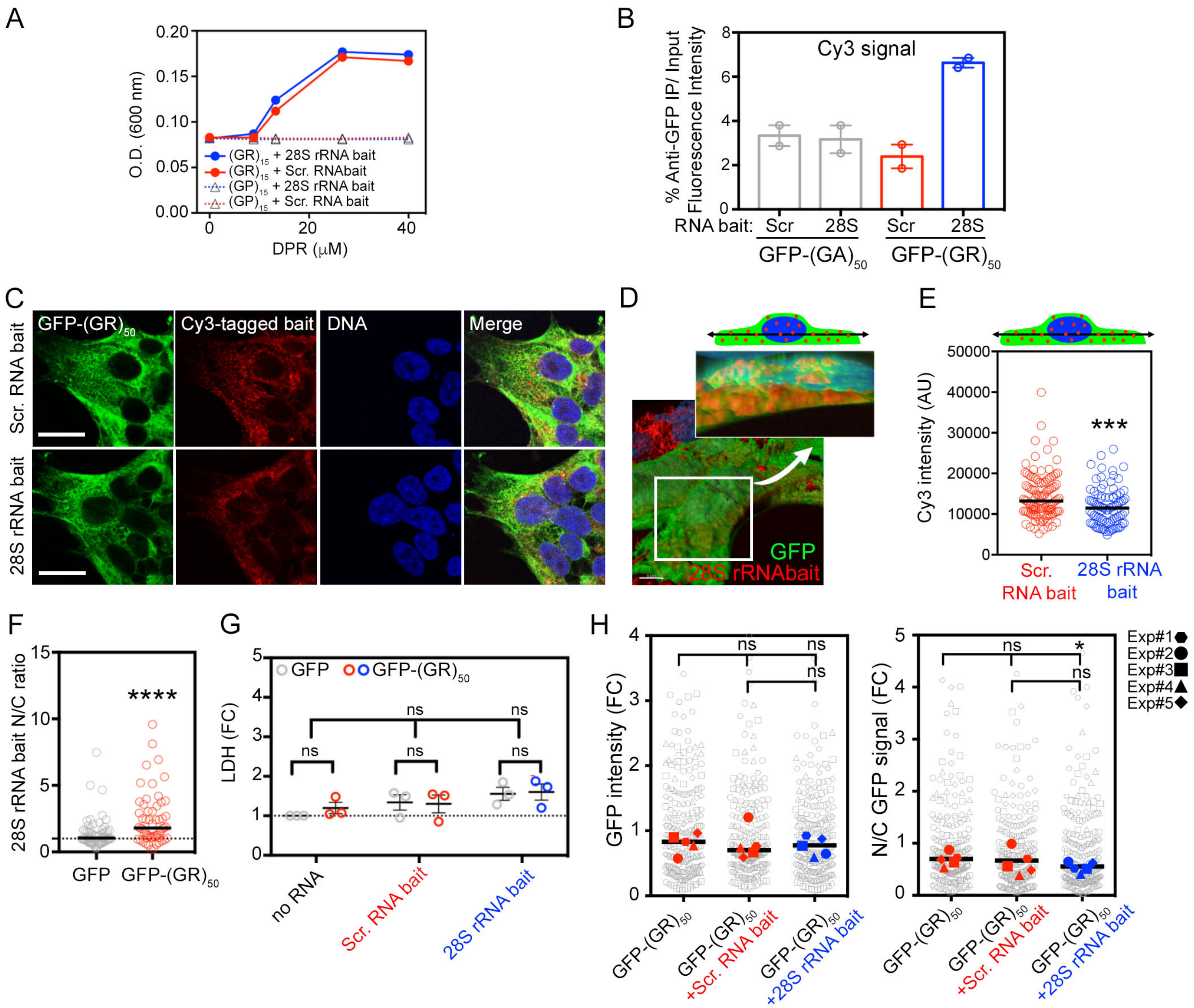
A
O.D. (600 nm)
0.20
0.15
0.10
0.05
0.00
0
20
40
DPR (μM)
(GR)15 + 28S rRNA bait
(GR)15 + Scr. RNAbait
(GP)15 + 28S rRNA bait
(GP)15 + Scr. RNA bait
B
% Anti-GFP IP/ Input Fluorescence Intensity
Cy3 signal
8
6
4
2
0
RNA bait:
Scr
28S
Scr
28S
GFP-(GA)50
GFP-(GR)50
C
GFP-(GR)50
Cy3-tagged bait
DNA
Merge
Scr. RNA bait
28S rRNA bait
D
GFP
28S rRNAbait
E
Cy3 intensity (AU)
50000
40000
30000
20000
10000
0
***
Scr. RNA bait
28S rRNA bait
F
28S rRNA bait N/C ratio
15
10
5
0
****
GFP
GFP-(GR)50
G
LDH (FC)
5
4
3
2
1
0
GFP
GFP-(GR)50
ns
no RNA
Scr. RNA bait
28S rRNA bait
H
GFP intensity (FC)
4
3
2
1
0
ns
GFP-(GR)50
GFP-(GR)50 +Scr. RNA bait
GFP-(GR)50 +28S rRNA bait
N/C GFP signal (FC)
5
4
3
2
1
0
ns
*
Exp#1⬢
Exp#2●
Exp#3■
Exp#4▲
Exp#5◆

Supplementary Figure 8. Modified RNA-based strategy to inhibit the toxic effects of poly-GR on ribosomal homeostasis.

A. Line graph depicting $(GR)_{15}$ and $(GP)_{15}$ concentration-dependent precipitation of scrambled and 28S rRNA baits calculated by optical density.

B. Lysates of HEK-293 cells co-transfected with Cy3-labeled scrambled or 28S rRNA baits and GFP-$(GA)_{50}$ or GFP-$(GR)_{50}$, were subjected to IP with an anti-GFP antibody. Bar graph showing the level of Cy3-labeled bait detected within the immunoprecipitates normalized to input.

C. Confocal images of HEK-293 cells sequentially co-transfected with scrambled or 28S rRNA baits, conjugated with Cy3 (red), and GFP (green). Hoechst 33342 was used to counterstain nuclei. Scale bar= 20μm.

D. Volumetric reconstruction of confocal images of HEK-293 cells sequentially co-transfected with 28S rRNA bait, conjugated with Cy3 (red), and GFP (green). Hoechst 33342 was used to counterstain nuclei. Scale bar=10μm. Inset shows a single plane reconstruction of GFP and Hoechst 33342 signal in combination with volumetric Cy3-bait signal.

E. Dot plot showing the total intensity of the signal associated to scrambled or 28S rRNA baits, conjugated with Cy3, in GFP-transfected HEK-293 cells. Bars represent median. Mann-Whitney U test, $p^{***}<0.001$.

F. Dot plot showing the nuclear/cytosolic (N/C) distribution of the 28S rRNA bait conjugated with Cy3 in GFP- or GFP-$(GR)_{50}$-transfected HEK-293 cells. Individual cells are represented as dots from 3 independent experiments and bars represent median. Mann-Whitney U test, $p^{****}<0.0001$.

G. Dot plot showing the fold change (FC) levels of LDH in the media of HEK-293 cells sequentially co-transfected with scrambled or 28S rRNA baits and GFP- or GFP-$(GR)_{50}$. Average values of each experiment are represented as dots and the dotted line marks the median in no RNA bait treated GFP-transfected cells. n=3 independent biological replicates; bars represent mean ± SEM; ANOVA, ns, not significant.

H. Dot plots showing the intensity (left) and N/C distribution (right) of GFP signal in GFP-$(GR)_{50}$-transfected HEK-293 cells upon treatment with scrambled or 28S rRNA baits. Individual cells from 3 experiments are represented by distinct shaped symbols in grey, median values of each experiment are represented by distinct shaped symbols in color, and bars represent the global median per condition. Multiple Comparisons of Means: Tukey Contrasts, $p^{*}<0.05$; ns, not significant.

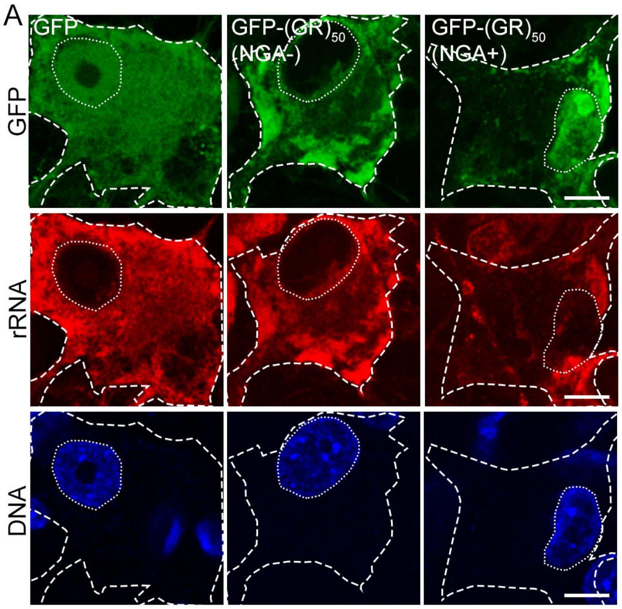
A
GFP
GFP-(GR)$_{50}$ (NGA-)
GFP-(GR)$_{50}$ (NGA+)
GFP
rRNA
DNA

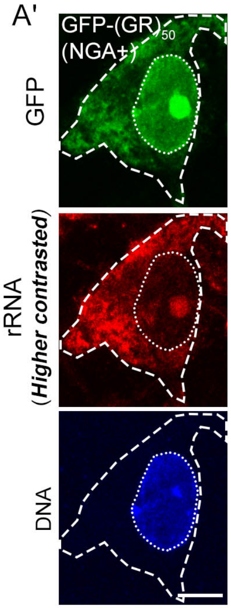
A'
GFP-(GR)$_{50}$ (NGA+)
GFP
rRNA (*Higher contrasted*)
DNA

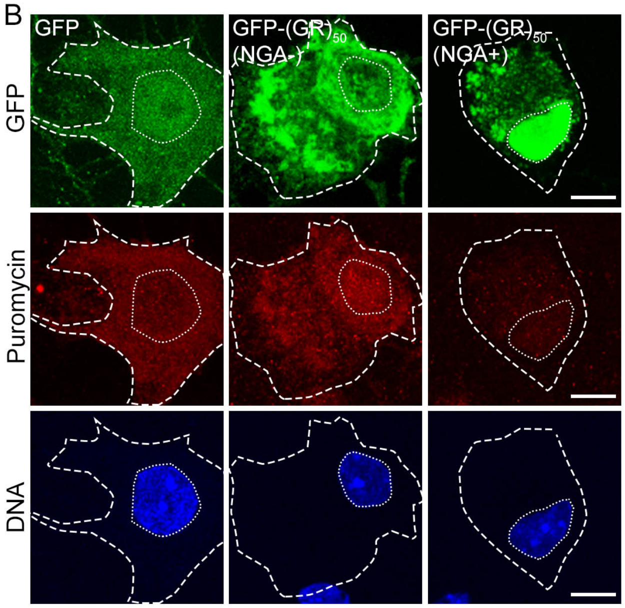
B
GFP
GFP-(GR)$_{50}$ (NGA-)
GFP-(GR)$_{50}$ (NGA+)
GFP
Puromycin
DNA

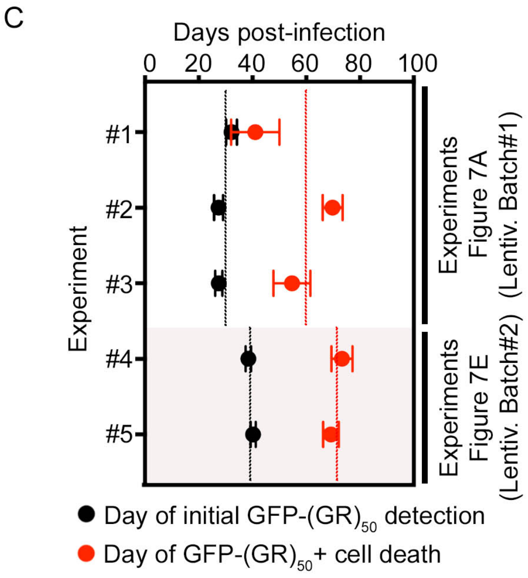
C
Days post-infection
0
20
40
60
80
100
Experiment
#1
#2
#3
#4
#5
Experiments Figure 7A (Lentiv. Batch#1)
Experiments Figure 7E (Lentiv. Batch#2)
● Day of initial GFP-(GR)$_{50}$ detection
● Day of GFP-(GR)$_{50}$+ cell death

Supplementary Figure 9. RNA-based strategy to inhibit the toxic effects of poly-GR in stem cell derived MNs.

A. Confocal images of GFP- and GFP-$(GR)_{50}$-transduced iPSC-derived MNs, with or without NGA, immunolabeled for rRNA at 80 days post-infection (dpi). Hoechst 33342 was used to counterstain nuclei. A', Image of a GFP-$(GR)_{50}$-transduced iPSC-derived MN with nucleolar NGA where the contrast in rRNA intensity was increased to enable the observation of nucleolar rRNA. Scale bars=10 μm.

B. Confocal images of GFP- and GFP-$(GR)_{50}$-transduced iPSC-derived MNs, with or without NGA, immunolabeled for puromycin at 80 days post-infection (dpi). Hoechst 33342 was used to counterstain nuclei. Scale bar = 10 μm.

C. Dot plot graph displaying the average post-infection day for initial expression of GFP-$(GR)_{50}$ and cell death across experiments. Dashed lines indicate average values of each metric across experiments and lentiviral batches. The time between GFP-$(GR)_{50}$ expression and cell death is preserved across experiments.

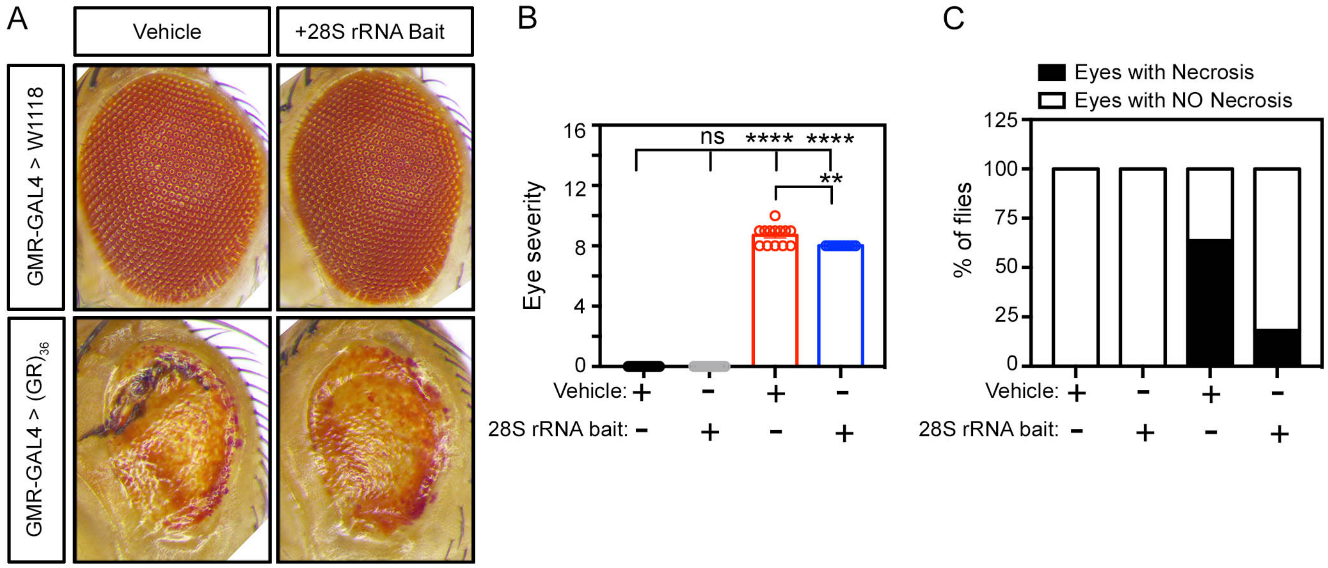

Supplementary Figure 10. RNA-based strategy to inhibit the toxic effects of poly-GR *in vivo*.

A. Representative eye images from (GMR-GAL4 x W1118) and (GMR-GAL4 x $(GR)_{36}$) mutant flies treated or non-treated with 28S rRNA-based bait.

B. Bar graph displaying the level of eye degeneration in the different conditions as referred to A. Each dot represents values of a single fly. ANOVA test, p**<0.01; p****<0.0001; ns, not significant.

C. Graph bar showing the percentage of (GMR-GAL4 x W1118) and (GMR-GAL4 x $(GR)_{36}$) flies with or without eye necrosis.

Descriptive Caption for Supplementary Tables

Supplementary Table 1. Computational raw data of RMSD, Rg, Intramolecular interaction, AP, and SASA analyses of the distinct DPRs characterized in this study.

Supplementary Table 2. Features annotated for each peak detected in CLIP-Seq analysis in GFP-$(GR)_{50}$ to GFP comparisons.

Supplementary Table 3. Metanalysis of previous anti-poly-GR IP-MS experiments. The table includes a detailed description of the ribosomal proteins that immunoprecipitated along with poly-GR in 7 different studies.

Supplementary Table 4. Computational raw data of RMSD, RMSF, Rg, SASA, and binding energies' analyses of a mammalian ribosome in the presence or absence of R-DPRs.

Supplementary Table 5. Secondary conformation analyses of 28S rRNA-based and scrambled baits. Secondary structures were obtained through 3 independent simulation methods.

Supplementary Table 6. Donor information and karyotyping results for the iPSC lines utilized in this study.